Journal of Power Sources 660 (2025) 238573

Contents lists available at ScienceDirect

Journal of Power Sources

journal homepage: www.elsevier.com/locate/jpowsour

Evaluation of SOEC segmented performance through experimental localized fuel electrode multisampling technique

Francesco Marino [a,b,*], Davide Pumiglia [b], Francesca Santoni [b], Maria Anna Murmura [c], Luca Simonetti [b], Viviana Cigolotti [b], Giulia Monteleone [b], Elio Jannelli [a]

[a] Department of Engineering, Università degli Studi di Napoli Parthenope, 80133, Napoli, Italy
[b] Laboratory for Hydrogen and New Energy Vectors (H2V), Division of Technologies and Vectors for Decarbonization (DEC), Department of Energy Technologies and Renewable Sources (TERIN), ENEA Italian National Agency for Energy, New Technologies and Sustainable Economic Development, 00123, Rome, Italy
[c] University of Rome "La Sapienza", Department of Chemical Engineering Materials and Environment, Via Eudossiana 18, 00184, Rome, Italy

HIGHLIGHTS

- 11-point multisampling setup can map SOEC local gas and temperature profiles.
- Electrochemical–thermal model predicts local current, voltage, and temperature.
- Peak current density of 0.45 A/cm^2 found near the inlet under all conditions.
- Localized diagnostics essential for SOEC performance and durability.

ARTICLE INFO

Keywords:
Solid oxide electrolysis
Multisampling SOEC
Electrochemical characterization

ABSTRACT

In this study, a commercial solid oxide electrolysis cell (SOEC) was tested under different operating conditions to evaluate electrochemical performance and thermochemical gradients at the fuel electrode. An innovative test bench with eleven sampling points distributed across the electrode surface enabled in-operando measurements of gas composition and temperature, uncovering performance gradients not detectable by conventional inlet–outlet analysis.

Experiments were carried out on a fuel-electrode-supported cell (81 cm^2 active area), varying inlet flow rate and composition. A simplified electrochemical–thermal model, developed from experimental data and fundamental electrochemical and thermodynamic principles, was validated and used to predict local voltage, current density, and temperature distributions.

The results indicate high electrochemical activity near the inlet, with local current densities up to 0.45 A/cm^2 and thermal gradients of about 4.5 °C across the cell surface.

Overall, the study provides new insights into the spatial heterogeneity of SOEC operating parameters and underscores the relevance of localized diagnostics. Such approaches improve the understanding of electrochemical and thermal behavior, supporting strategies to enhance SOEC efficiency and durability.

1. Introduction

Over the past few years, researchers have been studying a variety of solutions to the current issues related to the harmful pollutant emissions, and hydrogen appears to be a valid candidate for such purposes [1]. Hydrogen has received extensive attention as a clean energy carrier, and most likely it will be an important part of the energy mix in a low-carbon future [2]: in terms of efficiency of the future energy paradigm, the implementation of a widespread hydrogen technology seems to be crucial due to its being carbon free and its potential in storability and transportability [3].

From a scientific point of view, the most efficient and environmentally friendly hydrogen production method is through water splitting by means of electricity coming from renewable energy sources. Alternatively, production from less conventional electrolysis (such as co-electrolysis of water and CO$_2$ or fuel-assisted electrolysis) is a major

---

* Corresponding author. Department of Engineering, Università degli Studi di Napoli Parthenope, 80133, Napoli, Italy.
E-mail address: francesco.marino005@studenti.uniparthenope.it (F. Marino).

https://doi.org/10.1016/j.jpowsour.2025.238573
Received 4 August 2025; Received in revised form 19 September 2025; Accepted 5 October 2025

object of study as well. In spite of a few technical limitations, SOEC technology is certainly a valuable competitor on the market. The operation at such high temperatures (between 600 and 1000 °C) allows SOECs to be capable of having very high electrical-to-chemical energy conversion efficiencies thanks to good reaction kinetics [4] and of being able to produce syngas or methane from steam and CO_2, which can be further converted to liquid fuels through the Fischer-Tropsch process [5]. Moreover, other advantages such as scalability and flexibility to multiple inlet fuel types further increase their technological relevance [6–10].

While many studies have focused on SOEC performance and durability at stack-level [11–16], single cell-level investigations remain essential to understand localized phenomena and degradation mechanisms.

Several works have explored long-term operation and accelerated stress testing, highlighting the influence of operating conditions on performance and stability: Tietz et al. [17] successfully completed a test campaign on an electrode-supported solid oxide cell operated for 9000 h in SOEC mode with 80 % humidification and with a current density of $-1\ A/cm^2$, and a cell voltage degradation rate of 3.8 %/kh was observed. Königshofer et al. [5] instead opted for the development of accelerated stress test protocols in SOEC mode, with a water concentration and current density varying from 15 % to 90 % and from 0.250 A/cm^2 to 0.900 A/cm^2 respectively. The cell was kept in operation for about 200–300 h in continuously variable conditions, each presenting different kinds and degrees of impact on performance and microstructure of the cell. Nguyen et al. [4] performed long term ageing tests of a two-cell planar electrode supported stack in steam electrolysis (3450 h), co-electrolysis (640 h) and fuel cell operation (4000 h). Nearly no degradation after 2000 h of steam electrolysis (800 °C, $H_2/H_2O = 1/1$, FU = 15 %) at current density of $-0.3\ A/cm^2$ was observed.

Cell degradation is a phenomenon influenced by multiple factors, some of which can be attributed to the cell fabrication process [18,19] or to pinch-up, a factor excluded in this work due to the absence of geometric obstacles or cross-sectional restrictions in the gas channels. Despite the encouraging progress demonstrated in literature, cell degradation, proved to be adversely influenced by gas concentration and temperature gradients [20], is still considered one of the major concerns in SOEC technology [11,18,21]: as Wolf et al. [22] proved, their 1000 h-test at $-1A/cm^2$ and 800 °C showed a 370 mV/kh voltage increase, as well as the delamination of the LSC electrode and a partial Ni depletion in the active layer. To address these issues, Tong et al. [23] developed and tested a nano-engineered SOC featuring a gadolinium-doped ceria (CGO) nanogranular coating on the fuel electrode and a CGO scaffold on the air electrode, in order to improve both performance and degradation behavior. They achieved high performance and durability (voltage decrease of only 0.024 V/kh after 900 h at 1 A/cm^2), demonstrating that the CGO coating suppresses Ni migration while preserving the structure of active sites. Regarding cell degradation, the long-term 23 kh test by Schefold et al. [24] highlights a key factor, namely the partially different response of electrolyte-supported cells under prolonged stress: impedance spectroscopy reveals a predominantly ohmic degradation, attributable to the loss of ionic conductivity in the electrolyte, while the fuel electrode shows no significant signs of deactivation.

One of the approaches that allows to improve the performance and minimize the degradation is the optimization of the thermal and gas composition gradients distribution. On one hand, computational models are an effective method to predict the behavior of every portion of the cell as a function of its operating conditions. 1D and 2D models are mainly used to describe the I-V characteristic of a SOEC, whereas 3D models can provide detailed concentration of gas species and temperature distribution [25]. A few 3D model-related articles are retrievable in literature, developed to study impacts of operating conditions on SOECs, such as nominal working temperature, inlet gases compositions and gas flow field patterns [26–30].

On the other hand, experimental studies on localized cell behavior and performance allow the validation of the numerical models and confirm the presence of the phenomena predicted by the models.

The analysis of segmented SOCs has been reported in several studies, including that of Schiller et al. [31], who employed a planar, fuel-electrode-supported SOFC divided into 16 galvanically isolated segments for local experimental measurements, complemented by a 2D electrochemical model for comparison. This study revealed pronounced gradients of gas concentration and current density along the fuel electrode side of the cell, whereas the air electrode side exhibited much smaller gradients. Additional investigations on fuel cell operation have been conducted, including those by Wu et al. [32], Kim et al. [33], and Lang et al. [34].

With regard to SOEC operation, Moussaoui et al. [35] employed a segmented experimental setup to analyze the local electrochemical and thermal behavior of a commercial solid oxide cell. Their configuration partitioned the oxygen electrode into 20 segments, each individually controlled by an electronic load under both galvanostatic and potentiostatic modes, enabling the measurement of voltage and current density for each segment. Königshofer et al. [36] tested cells with a segmented air electrode under steam electrolysis and co-electrolysis conditions, with the aim of experimentally investigating local impedance and degradation characteristics.

Through this study, the authors assess the localized temperature and gas concentration distribution within an SOEC using a custom experimental setup comprised of 11 sampling points. By analyzing these data and applying thermodynamic principles, valuable insights into the electrochemical performance of the cell are obtained. The objective of this study is not to develop complex fluid dynamic models for the precise determination of all possible variables but rather to derive results that provide a qualitative understanding of the underlying phenomena at play and their directional trends. Thus, the aim is to demonstrate that, with a simple yet innovative experimental setup, it is possible to extract extensive information regarding the cell's operation across its entire surface, thereby providing insights into the effects of these phenomena on degradation and durability.

In this context, previous studies have already demonstrated the effectiveness of a similar multisampling setup in fuel cell mode, focusing on the fuel-electrode surface under various operating conditions. In particular, Santoni et al. [37] and Pumiglia et al. [38] employed this configuration to investigate the local gas-phase composition and temperature distribution in SOFCs fed by reformate natural gas. Conti et al. [39] also used this setup for combined experimental-modeling studies. These works laid the foundation for the present study, which extends the application of the multisampling approach to SOEC operation, enabling a detailed spatial analysis of electrochemical and thermal behavior under electrolysis conditions. The main differences with respect to previous studies conducted on a similar setup lie firstly in the operation of the test bench under electrolysis mode (thus involving much higher water content, particularly at the inlet), which requires more accurate thermal management of the gas mixture in the sections upstream of the cell. Secondly, the extension includes cell fictitious segmentation as well as the development of simplified electrochemical and thermal predictive models, aimed at determining the local distribution of current density, voltage, and temperature.

2. Materials and methods

In this work, a SOEC single cell has been tested in various operating conditions, following an accurate definition of the experimental campaign aimed at evaluating the cell electrochemical performances while investigating, at the same time, the distribution of thermochemical gradients at the fuel electrode by means of a specific test bench layout. Within this section, a comprehensive description of the laboratory equipment, cell characterization approach and test campaign definition are provided.

2.1. Single cell and test rig design

The experiments in this study have been performed on a commercial fuel electrode-supported SOC single cell (with Ni-YSZ/YSZ/GDC/GDC-LSCF structure), operated in electrolysis mode, whose dimensions are 10 × 10 cm^2 with an active area of 81 cm^2.

The system is equipped with a temperature-programmed furnace, where the cell housing is placed, in order to reach the desired operating temperature, maintained constant throughout the duration of the test runs.

The in-house built cell set-up, represented in Fig. 1, hereafter referred to as *multisampling set-up*, consists of two compartments where the inlet gas, both fuel- and air-side, is initially carried in a 12 mm-diameter circular section pipe, and then split in three smaller pipes with a diameter of 6 mm. Fuel and air are fed to the cell in co-flow configuration. The fuel distribution is realized by two almost identical plates (one for the fuel-side and the other for the air-side), with the only feature differing the two being the presence of 11 holes for the fuel-side gas and temperature sampling. The plates have a pre-chamber that favors gas build-up and hence distribution throughout the cell surface.

The multisampling setup allows temperature and gas compositions measurements across the cell in 11 sampling spots that cover a wide portion of its surface. Temperature monitoring is realized via type K thermocouples, whose nominal error is about ±1 °C.

Gas composition is accomplished via a gas chromatograph (Clarus 680-Perkin Elmer) equipped with specific column for the compounds studied (Haysep Q and molecular sieve5A) and a thermal conductivity detector (TCD). The gas sampling capillaries (1/16″ stainless steel) are all heated above 100 °C along their entire length up to the GC inlet, in order to avoid condensation of steam in the lines. The withdrawal flow rate was maintained at 5–10 mL/min per channel, controlled via calibrated mass flow controllers, corresponding to less than 2 % of the local fuel flow and thus not affecting the electrochemical operation of the cell. The system was calibrated with certified gas mixtures, and repeatability was verified at multiple sampling points. Based on the manufacturer's technical specifications, the typical accuracy for binary gas mixtures is on the order of ± 2–3 vol%: ±3 %vol is the value adopted as the reference for error propagation in the estimation of steam conversion.

Additionally, the test rig is equipped with an electronic load (Kikusui 43 PLZ664WA) connected in series with a power supply (Delta Elektronika SM-30-100D), a SCADA system for data acquisition and an electrochemical impedance analyzer (BioLogic BP-300), all ensuring detailed in-operando analysis.

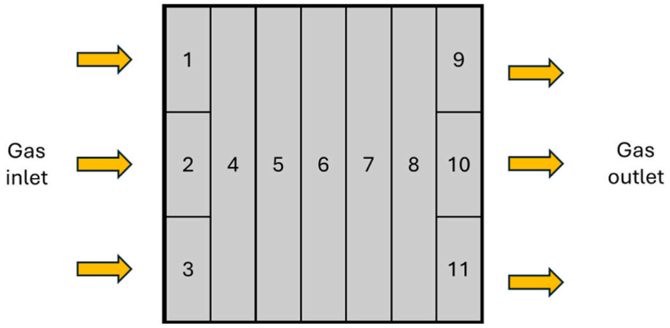

Fig. 2. Fictitious partitioning of the fuel electrode into 11 areas, top view.

The concept of a partitioned single cell is depicted in Fig. 2. For detailed localized analyses, the fuel electrode is figuratively divided into 11 segments, hence each of them is assigned to each of the sampling points. Areas are divided in accordance with how the sampling points are distributed across the cell and are named after the sampling spot they surround. Surface areas are 3.857 cm^2 for inlet and outlet points, and 11.571 cm^2 for all the other points, resulting in an overall 81 cm^2 area. Table I reports the distance of each sampling point from the inlet cross section of the cell. Due to the presence of the premixing chamber, the gas enters the cell homogeneously along the y-axis and is distributed over the cell surface through 15 distribution channels. As a result, the total inlet flow to the cell is automatically and uniformly divided among the fictitious segments 1, 2, and 3, each receiving one third of the total flow. Segments 4–8, instead, extend across the entire cell along the y-axis and are therefore exposed to the full inlet flow. Similarly, the outlet segments (9, 10, 11) each receive one third of the total flow. On this basis, a homogeneous gas flow distribution along the cell y-axis is assumed.

Table 1
Distance of sampling point from the inlet.

Sampling point	Distance (mm)
1, 2, 3	9
4	21
5	33
6	45
7	57
8	69
9, 10, 11	81

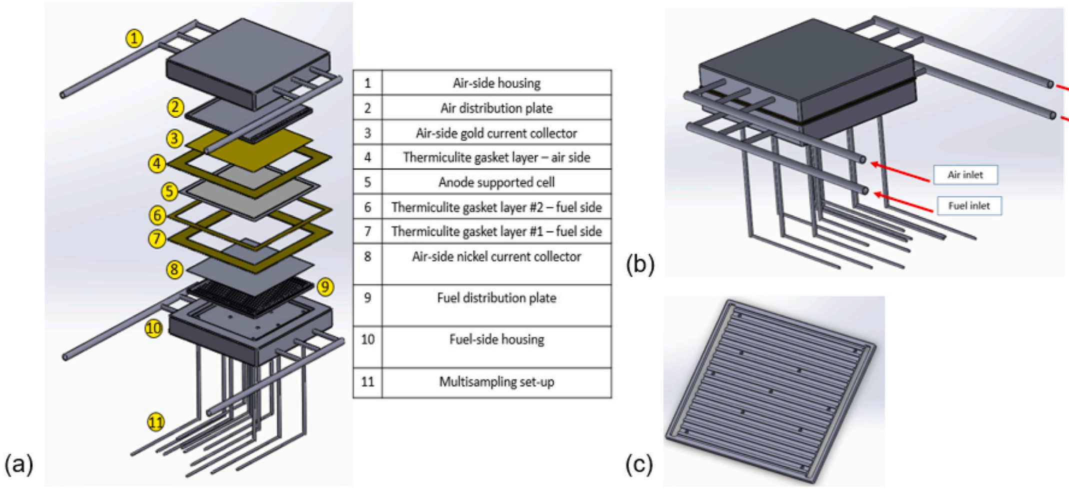

1	Air-side housing
2	Air distribution plate
3	Air-side gold current collector
4	Thermiculite gasket layer – air side
5	Anode supported cell
6	Thermiculite gasket layer #2 – fuel side
7	Thermiculite gasket layer #1 – fuel side
8	Air-side nickel current collector
9	Fuel distribution plate
10	Fuel-side housing
11	Multisampling set-up

Fig. 1. Exploded view of the test setup (a); Exploded view of the test setup – focus on the gas flows (b); fuel-side gas distribution plate (c).

2.2. Single cell preliminary characterization procedures and test campaign definition

Electrical resistance and gas tightness tests are performed on the single cell prior to its standard start-up procedure and reduction, with the leakage resulting to be in the range 2–4 % of the inlet flow rate (500 mL/min of N_2) – a value considered acceptable to carry on with the tests. Its initial performances are evaluated in fuel cell mode. Silva-Mosqueda et al. [40] have already previously conducted an experimental campaign on a Solid Oxide Intermediate Temperature electrode-supported single cell using a similar version of the test bench, effectively validating the current test rig and cell assembly.

Once the benchmark performances are assessed, hence the test bench is validated, the single cell is tested by performing polarization curves, Electrochemical Impedance Spectroscopy (EIS), short-term stability tests (at least 2 h in stable operation) and gas chromatographic analysis under different operating conditions. In order to map the performances in a wide operating window, tests are run at different:

- Total fuel flow rates (300–500 mL/min);
- Fuel compositions (50/50–70/30H_2O/H_2 %vol)

The electrochemical activity of the electrodes was monitored at a DC bias current of 1 A, with an AC perturbation of 10 mA applied over a frequency range from 10 mHz to 100 kHz. The I–V curves have been performed taking into account a few constraints: steam utilization below 90 % (to avoid induced cell degradation), maximum cell voltage 1300 mV [41], maximum current density 0.5 A/cm^2 (nominal operating point suggested by the manufacturer), scan rate set to 0.1 A/s and a stabilization time of 1 min every time the new current load was reached (e.g. 1 A, 2 A, 3 A, etc.)

In Table II all the experimental conditions tested are summarized, while in Fig. 3b the plots of cell voltage in the stabilization process are reported.

The experimental steps carried out are the following: in OCV conditions one parameter is changed with respect to the previous test (e.g. total flow rate, gas composition, temperature) and sufficient time for the system to stabilize in its new working condition is given; the EIS test is then performed, followed by the IV curve up to a current value at which either the voltage reached 1300 mV (threshold under which the operation in SOEC was considered safe with no forced degradation induced), or Fuel Utilization reached 90 %, or a current density of 0.5 A/cm^2 was reached. The cell was then kept at selected load value of 0.235 A/cm^2 (or 19 A) for a minimum of 2h. After the stabilization period under load, the open circuit conditions are restored, and the new parameters of the subsequent tests are set.

The EIS spectra, primarily intended for the preliminary monitoring of cell performance, are shown in Fig. 3a. A decrease in polarization resistance is observed with increasing inlet steam content, whereas the ohmic resistance, being unaffected by the feed composition, remains nearly constant in all three cases at a value between 0.20 and 0.25 Ω cm^2.

This value is consistent with other studies conducted on SOECs, such as Wolf et al. [22], whose work reports internal resistance values around 0.2 Ω cm^2. Studies with segmented cells, on the other hand, exhibit ohmic contributions ranging between 0.3 and 0.4 Ω cm^2 per segment, higher than those observed for the full cell due to the complex architecture of the setup, which prevents perfectly flat contact between the segments and the interconnect [35,36].

Table 2
Experimental working conditions for the 81 cm^2 electrode-supported single cell.

Condition no.	Total fuel flow rate	H_2	H_2O
1	300 mL/min	150 mL/min (50 % vol)	150 mL/min (50 % vol)
2	500 mL/min	250 mL/min (50 % vol)	250 mL/min (50 % vol)
3		150 mL/min (30 % vol)	350 mL/min (70 % vol)

2.3. Cell voltage prediction model (V)

The electrochemical reactions occurring in steam electrolysis (SOE) mode at the electrodes-electrolyte interfaces are presented in Table III. At the cathode (fuel electrode) steam is reduced to form hydrogen and oxygen ions by gaining electrons coming from the anode. At the anode (air electrode) oxygen ions coming from the cathode migrate through the electrolyte and are oxidized to form molecular oxygen, releasing electrons.

Cell potential, as a function of the current load, can be expressed as [42–45]:

$$V = V_{Nernst} + \eta_{act} + \eta_{ohm} + \eta_{conc} \tag{1}$$

where V_{Nernst} [V] is the Nernst (reversible) cell potential, η_{act} [V] is the activation polarization, η_{ohm} [V] is the ohmic polarization and η_{conc} [V] is the concentration polarization.

The reversible cell potential is given by the Nernst equation [42,46]:

$$V_{Nernst} = E_0 - \frac{R \cdot T}{2 \cdot F} \cdot ln\left(\frac{p_{H_2O}}{p_{H_2} \cdot {p_{O_2}}^{0.5}}\right) \tag{2}$$

$$E_0 = 1.253 - 2.416 \cdot 10^{-4} \cdot T \tag{3}$$

where E_0 [V] is the reversible cell potential at standard pressure and temperature, T [K] is the cell temperature, R [J mol^{-1} K^{-1}] is the universal gas constant, F is the Faraday's constant [96487C/mol] and p_x is the x species partial pressure.

The activation overpotential is split into fuel-electrode and air-electrode overpotential [42]:

$$\eta_{act,fuel} = \frac{2 \cdot R \cdot T}{2\,F} \cdot \sinh^{-1}\left|\frac{i}{2 \cdot \gamma_{fuel} \cdot \left(y_{H_{2,IN}}\right)^{A} \cdot \left(y_{H_2O_{,IN}}\right)^{B} \cdot e^{-\frac{E_{act,fuel}}{R \cdot T}}}\right| \tag{4}$$

$$\eta_{act,air} = \frac{2 \cdot R \cdot T}{2\,F} \cdot \sinh^{-1}\left|\frac{i}{2 \cdot \gamma_{air} \cdot \left(y_{O_{2,IN}}\right)^{C} \cdot e^{-\frac{E_{act,air}}{R \cdot T}}}\right| \tag{5}$$

$$\eta_{act,tot} = \eta_{act,fuel} + \eta_{act,air} \tag{6}$$

where γ_{fuel} and γ_{air} [A/cm^2] are pre-exponential coefficients in exchange current densities, $y_{x,IN}$ [%] are the molar inlet fractions of the species x, A, B and C [−] are the reactant kinetic orders, $E_{act,\,fuel}$ and $E_{act,air}$ [J/mol] are the activation energies at the fuel- and the air-electrode, i is the current density [A/cm^2].

The ohmic overpotential is defined as in Eq. (7) [42]:

$$\eta_{ohm} = P_1 \cdot T \cdot e^{\frac{P_2}{T}} \cdot i \tag{7}$$

where P_1 [Ω cm^2 K^{-1}] and P_2 [K] are empirical parameters specific for each case study.

The concentration (or diffusion) overpotential may be expressed with Eq. (10) [46]:

$$\eta_{conc,fuel} = -\frac{R \cdot T}{2 \cdot F} \cdot ln\left(1 - \frac{i}{i_{lim}}\right) \tag{8}$$

$$\eta_{conc,air} = -\frac{R \cdot T}{2 \cdot F} \cdot ln\left(1 - \frac{i}{i_{lim}}\right) \tag{9}$$

$$\eta_{conc,tot} = \eta_{conc,fuel} + \eta_{conc,air} \tag{10}$$

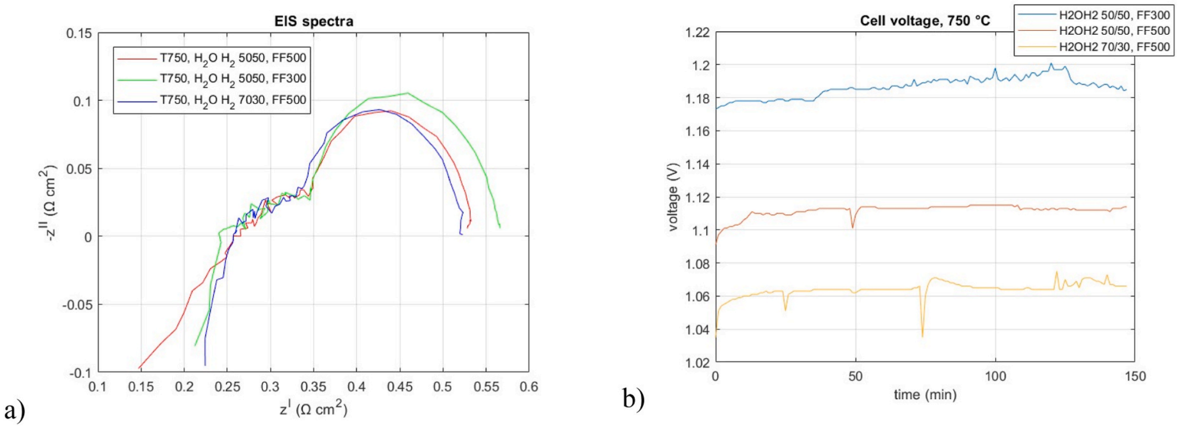

Fig. 3. a) EIS spectra for all testing conditions; b) cell voltage versus time in the stabilization process (>2 h) in all testing conditions.

Table 3
Electrochemical reactions in steam SOE mode.

Where	Reaction
Cathode (fuel electrode)	$H_2O + 2e^- \rightarrow H_2 + O^{2-}$
Anode (air electrode)	$O^{2-} \rightarrow \frac{1}{2}O_2 + 2e^-$
Global reaction	$H_2O \rightarrow H_2 + \frac{1}{2}O_2$

where i_{lim} (A/cm^2) is the limiting current density. In practice, given a certain inlet flow rate and composition, it corresponds to the current density at which 100 % of steam conversion is reached.

For the model, the values of the input parameters are summarized in Table IV:

Fig. 4 presents the voltage vs current density data obtained from both modeling simulations and experimental measurements, in all of the three working conditions studied. I-V curves exhibit consistent trends across the five different conditions, as both the predicted and measured maximum current input increase as the H_2O mass flow rate on the fuel side rises. The comparison reveals an accurate prediction of the cell voltage by the model, except at very high current densities where the prediction is overestimated (at steam conversion over 80 %). This does not undermine the validity of the model because, for the scope of this study, only current densities below or equal to the nominal value (0.25 A/cm^2) will be explored: in this operating range, the maximum relative error is 8 mV (or 6.1 %) given by condition no.1 at 0.25 A/cm^2. Moreover, it can be observed that the voltage calculated using the model is systematically higher than the voltage measured experimentally (up to 3 mV).

Table 4
Values of input parameters in the present study – calculation of cell voltage.

Parameter	Value	Reference	Unity
Temperature (T)	1023	–	K
Pre-exponential coefficient – fuel side (γ_{fuel})	5×10^5	[42]	A/cm^2
Pre-exponential coefficient – air side (γ_{air})	5×10^6	[42]	A/cm^2
Molar inlet fraction of H_2 ($y_{H2,IN}$)	30–50		%
Molar inlet fraction of H_2O ($y_{H2O,IN}$)	50–70		%
Reactant kinetic order (A)	0.5	[42]	–
Reactant kinetic order (B)	0.5	[42]	–
Reactant kinetic order (C)	0.25	[42]	–
Activation energy at the fuel electrode ($E_{act,\ fuel}$)	10^5	[42]	J/mol
Activation energy at the air electrode ($E_{act,air}$)	1.2×10^5	[42]	J/mol
Empirical parameter (P_1)	1.6×10^{-7}	adapted from [42]	Ω cm^2 K^{-1}
Empirical parameter (P_2)	7500	adapted from [42]	K
Limiting current density (i_{lim})	0.568–4.34		A/cm^2

Since the ideal gas assumption employed in this study (which uses partial pressures instead of fugacities in the calculation of the Nernst potential) is known to be highly accurate at atmospheric pressure [47], this discrepancy may instead be attributed to the method used for calculating the equilibrium constant in the determination of the reversible cell potential. This phenomenon has been reported in the literature for solid oxide cells [48], with discrepancies between the two values reaching up to 5 mV [47]. Another contributing factor may be the actual operating temperature: although the furnace is set to 750 °C, the inlet gases from the tank do not immediately reach the surrounding temperature (T < 750 °C), which, as shown in Eq. (2), leads to an increase in the Nernst potential.

While the predictive model presented here relies on classical electrochemical kinetics and transport formulations, it is important to note that several additional phenomena may affect the effective electrochemical response of the electrodes. These include local variations in the number and quality of contact points, electrode aspect ratio and morphology, as well as charge and ion accumulation in the vicinity of the electrode–electrolyte interfaces. Moreover, recent works have highlighted the role of surface configurations and reconstructions in Ni-based electrodes, which can induce a p-type semiconducting character and significantly modify the activation and transport processes at the electrode surface [49,50]. Although these effects are not explicitly included in the present simplified formulation, they represent crucial factors in interpreting deviations between experimental data and theoretical predictions, especially at high current densities or under strongly non-uniform operating conditions.

2.4. Determination of local cell current density

The following equation is defined:

$$I(x) = 2 \cdot F \cdot \dot{n}_{H_2O,cons}(x) \tag{11}$$

Where I (A) denotes the electric current, x (cm) represents the position along the gas flow path, $\dot{n}_{H_2O,cons}$ (mol/s) is the molar flow rate of water vapor consumed at position x. By applying the differentiation method, the following expression is obtained:

$$i(x) = 2 \cdot \frac{F}{W} \cdot \frac{d\dot{n}_{H_2O,cons}(x)}{dx} \tag{12}$$

Where i (A/cm^2) is the current density at position x, W is the width of the cell's active area. It can be observed that the current density at each point is a function of the cell size and the water conversion rate, which in

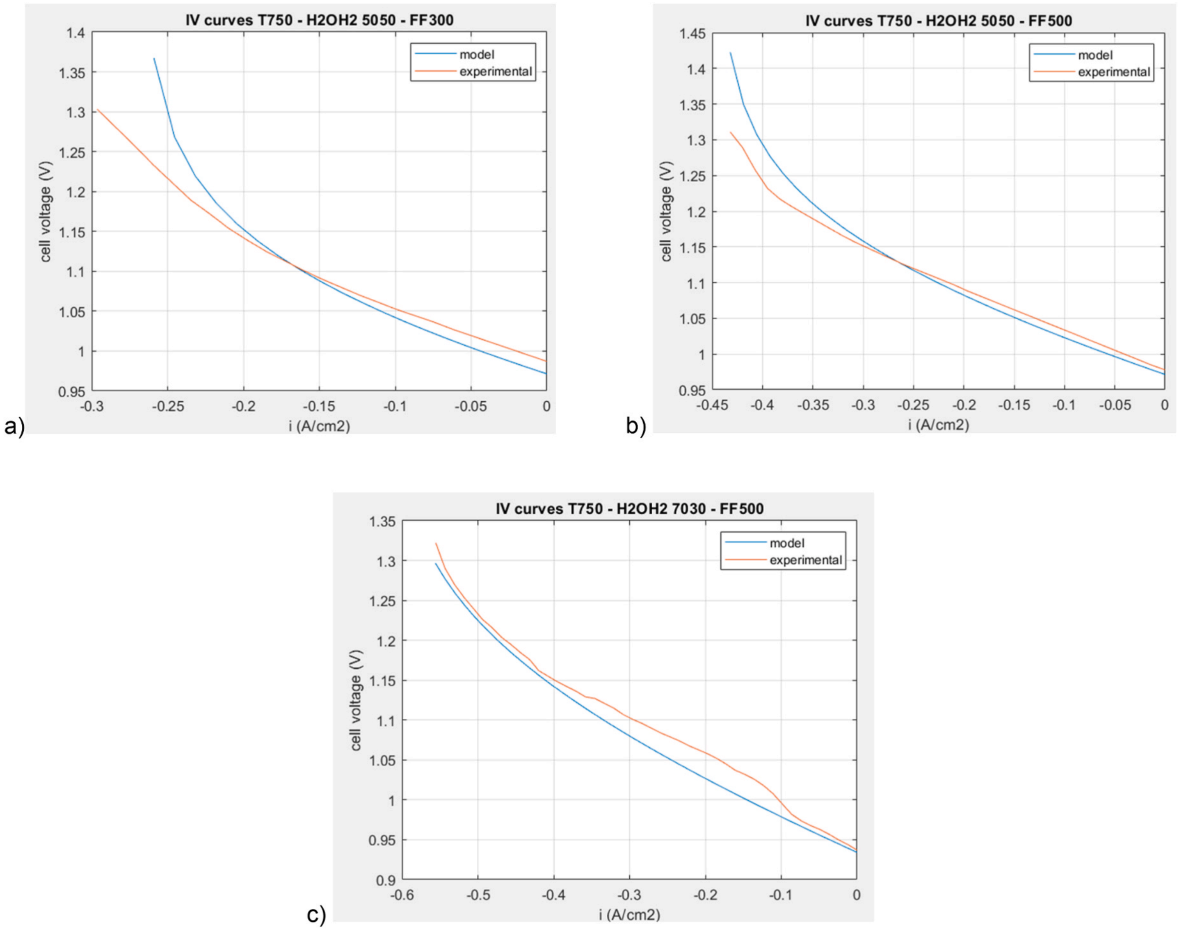

Fig. 4. Comparison of experimental and modeled polarization curve; as in Table II: a) condition no.1; b) condition no.2; c) condition no.3.

turn is derived from experimental gas chromatographic data. The finite number of experimental measurements does not allow for a continuous spatial distribution of current density; therefore, a fitting of the experimental points (indicating the water percentage) was performed in order to obtain a continuous curve. From this curve, it is possible to determine the water flow rate converted at each point.

It is also important to note that the equations presented are applicable at the macroscopic scale, and do not account for local phenomena or microstructural states.

2.5. *Determination of local cell voltage*

The validation of the model described in section 2.4 serves as a foundation for determining one of the primary objectives of this study: the distribution of cell voltage across its surface. As outlined in section 1.1, the cell is divided into 11 smaller segments. These segments can be considered as scaled-down versions of the complete cell, possessing identical characteristics while differing only in size. Consequently, under identical operating conditions, in this simplified approach these segments are considered to retain the same chemical and performance properties as the full cell from which they originate.

This assumption is deemed valid provided that the structural properties of the cell are uniform across its entire surface. Given that the tested cell has not undergone prior experimentation, it is reasonable to assume that its properties remain consistent across all segments. This ensures that the 11 segments described in section 1.1 function as true repeating units of the original full cell.

The model from section 1.1 is thus modified and the following input parameters, which vary depending on the case study, are provided to it, while the other structural parameters observed in the full cell remain unchanged:

- area of the cell segment
- local current density
- gas flow rate entering the cell segment
- gas composition entering the cell segment
- limiting current density

2.6. *Determination of local cell temperature*

The governing equations to describe the flow field are the Navier-Stokes equations [8,25,48]:

$$\frac{\partial \rho}{\partial t} + \nabla(\rho \cdot \overrightarrow{v}) = 0 \tag{13}$$

$$\rho\left[\frac{\partial \overrightarrow{v}}{\partial t} + (\overrightarrow{v} \cdot \nabla) \cdot \overrightarrow{v}\right] = -\nabla p + \mu \cdot \nabla^2 \overrightarrow{v} + \rho \cdot g \tag{14}$$

$$\rho \cdot c_p \cdot \left[\frac{\partial T}{\partial t} + \overrightarrow{v} \cdot \nabla T\right] = k \cdot \nabla^2 T + \dot{q} \tag{15}$$

Eqs. (13)–(15) are the mass, momentum and energy conservation equations respectively. Some simplifying assumptions are made:

- steady-state condition;
- c_p and h constant within each of the segments into which the full cell is divided;

- heat absorbed/generated constant within each of the segments into which the full cell is divided
- 1D temperature variation (along the x-axis)
- ideal gases
- negligible radiative heat transfer
- constant cell surface temperature

Based on these considerations, the Navier-Stokes equations are significantly simplified, leading to an analytical formulation of the temperature:

$$T_{g,j}(x) = T_s + \left(T_{g0,j} - T_s\right) \cdot e^{\left(\frac{-h \cdot P \cdot x}{\dot{m}_j \cdot c_{p,j}}\right)} - \frac{\dot{Q}_{cell,j} \cdot l}{h \cdot P} \cdot \left(1 - e^{\left(\frac{-h \cdot P \cdot x}{\dot{m}_j \cdot c_{p,j}}\right)}\right) \tag{16}$$

$$\dot{Q}_{cell} = \Delta H \cdot \dot{m}_{H_2O\ conv} - V_{cell} \cdot i \tag{17}$$

Where j is the cell segment object of study, $T_{g,j}(x)$ (K) is the gas temperature across the surface of segment j, T_s (K) is the cell surface temperature, $T_{g0,j}$ (K) is the gas temperature at the inlet of the segment j, h (W/m^2 K) is the convective heat transfer coefficient between cell surface and gas, P (m) is the perimeter of the cross section, x (m) is the distance from the inlet cross section of segment j, $\dot{m}_j$ (kg/s) is the total gas flow rate entering segment j, $c_{p,j}$ (J/kg K) is the specific heat capacity of the gas mixture in segment i, l (m) is the width of the cross section.

Eq. (16) hence indicates the gas temperature, as a function of the distance from the inlet section, in each of the 11 sub-cells.

As reported by Min et al. [51], the net amount of heat generation or consumption of a solid oxide cell can be defined with the formulation in Eq. (17), where Q_{cell} (W/cm^2) is the heat generation/consumption, V_{therm} (V) is the thermoneutral voltage, V_{cell} (V) is the cell voltage, ΔH (J/mol) is the enthalpy change during electrochemical reaction at the operating temperature, and $\dot{m}_{H2O\ conv}$ (mol/s) is the molar flow rate of water conversion in the electrochemical reaction. Based on the cell operating voltage, Q_{cell} can be positive or negative, indicating the operating characteristics of the SOEC:

$$\dot{Q}_{cell} \begin{cases} > 0 \text{ endothermic operation} \\ = 0 \text{ thermoneutral operation} \\ < 0 \text{ exothermic operation} \end{cases} \tag{18}$$

An entire subsection must be dedicated to the determination of h. The reason why only convective heat exchange has been considered is that, according to literature studies, in the case of planar solid oxide cells, heat transfer between the gas and the cell is predominantly convective, whereas radiative heat exchange becomes non-negligible only in tubular cells [52].

To the best of the authors' knowledge, studies on the magnitude of the convective heat transfer coefficient in planar solid oxide cells are absent in the literature. For this reason, the calculation is performed using formulas and correlations from thermodynamics, as reported below.

The convective heat transfer coefficient is calculated using Eq. (19) [53,54]:

$$h = \frac{Nu \cdot k}{L} \tag{19}$$

where:

- k (W/m·K) is the thermal conductivity of the gas mixture,
- L (m) is the specific length of the duct,
- Nu is the Nusselt number.

The latter depends on the flow type and the geometry of the gas duct. For rectangular cross-sections, as in the present case study, with a width-to-height ratio of around 3, the corresponding Nu value is 3.96 [53]. Based on these considerations, the value of h is determined: $h = 10.74$ W/m^2 K.

Table V reports the values of the parameters used for the thermal analysis. It is important to note that the value of h varies with the composition of the gas mixture, which becomes increasingly rich in H_2 and less rich in H_2O as the gas progresses. However, since the impact of this variation on the final result would not be significant and to avoid complicating the calculations, given the purpose of the work, h has been determined considering the inlet gas mixture.

The average gas velocity was estimated from the definition of volumetric flow rate, a known parameter:

$$Q = v \cdot w \cdot H \cdot n \tag{20}$$

Where Q (m^3/s) is the volumetric flow rate.

Reynolds number is reported in Table V as well, and is determined as follows:

$$Re = \frac{\rho \cdot v \cdot D_h}{\mu} \tag{21}$$

Since the Reynolds number is, for all case studies, well below the threshold for the flow to be considered turbulent [53], it can be concluded that the flow is assumed to be laminar.

3. Results and discussion

3.1. Experimental gas composition distribution

In Fig. 5 the experimental H_2 and H_2O concentration plots across the fuel-electrode surface are reported, along with their respective H_2O concentration contour plots, for the three conditions tested. Given the measurement uncertainty of the GC, error bars of ±3 vol% are shown, as indicated in Section 2.1.

In condition 1 ($H_2O/H_2 = 50/50$, FF = 300 mL/min), the H_2O concentration drops steeply from 50 % at the inlet to about 10 % at the outlet. The contour plot reveals a strong gradient concentrated in the first half of the cell, particularly between sampling points 1-2-3 and 4. This indicates that the majority of the electrochemical activity is localized near the inlet, where the steam concentration is highest. The distribution on the axis perpendicular to the direction of the flow also shows some slight asymmetry, suggesting non-uniform gas distribution across the width of the cell.

In condition 2 ($H_2O/H_2 = 50/50$, FF = 500 mL/min), the H_2O profile is more gradual, ranging from 50 % to about 25 %, as this condition mitigates the formation of steep gradients.

In condition 3 ($H_2O/H_2 = 70/30$, FF = 500 mL/min), the inlet steam concentration is higher (70 %), and the outlet still retains significant H_2O (about 40 %). The conversion is less pronounced, as expected under constant current operation with excess steam.

These results confirm that steam conversion is not uniform across the cell surface, and that the inlet region consistently exhibits the highest electrochemical activity. The extent and distribution of the gradients are

Table 5
Values of parameters– thermal analysis.

Parameter	value	unity
Nusselt number (Nu)	3.96	–
Thermal conductivity of gas mixture (k)	0.244	W/m K
Width of channels (w)	0.0047	m
Height of channels (H)	0.0016	m
Specific length of channels (L)	0.09	m
Width to height ratio (w/H)	2.95	–
Hydraulic diameter of channels (D_h)	0.0024	m
Gas velocity (v)	0.06 (case 1) – 0.1 (case 2–3)	m/s
Dynamic viscosity (μ)	$3.624 \bullet 10^{-5}$	Pa • s
Gas density (ρ)	0.0426	kg/m^3
Number of channels (n)	11	–
Reynolds number (Re)	0.17 (case 1) – 0.28 (case 2–3)	–

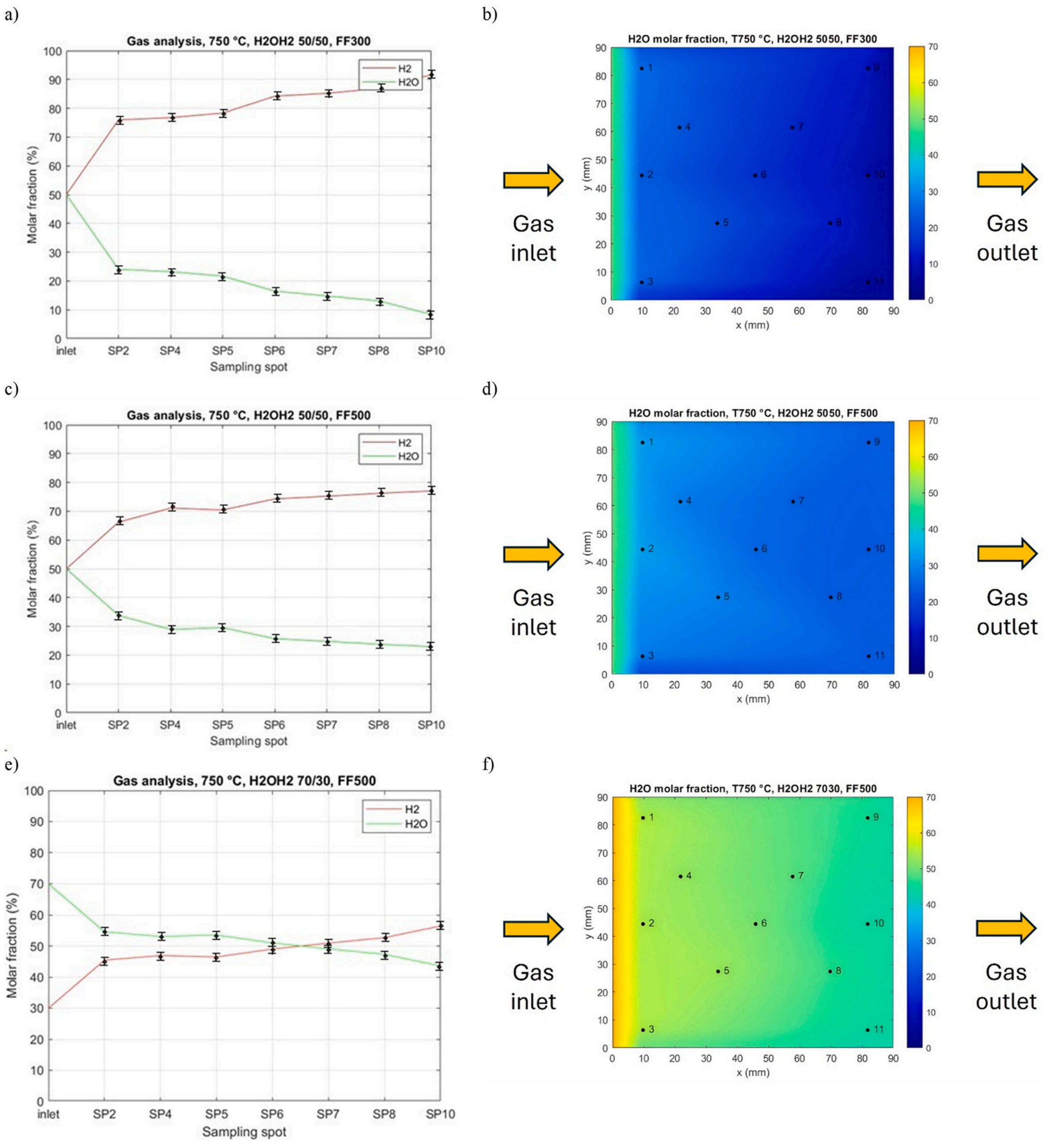

Fig. 5. H_2 and H_2O concentration plots; as in Table II: a) condition no.1; c) condition no.2; e) condition no.3.

strongly influenced by the inlet flow rate and composition: since the same amount of water needs be converted (electrical load remains unaltered), the outlet H_2O concentration varies depending on the inlet water content. In terms of gas composition, lower flow rates and lower steam content lead to sharper gradients, while higher flow rates and excess steam promote more uniform operation.

H_2O contour plots: b) condition no.1; d) condition no.2; f) condition no.2.

In order to show the correlation between experimental and theoretical results, a Faradaic balance on the hydrogen produced has been performed (Eq. (22)):

$$H_{2\ produced,Faradaic} = \frac{I}{2 \cdot F} \cdot 22.414 \cdot 60 \cdot 1000 \tag{22}$$

Where $H_{2\ produced,Faradaic}$ (ml/min) is the theoretical production of H_2 through the electrochemical conversion of water, I (A) is the current, 22.414 (Nl/mol) are the normal liters of any gas contained in a mole, 60 (s/min) and 1000 (ml/min) are conversion factors. Added to the inlet H_2 content, the overall H_2 content at the outlet can be determined. At experimental level, the percentage of H_2 at the outlet allows the calculation of the effective outlet H_2 content ($H_{2\ produced,exp}$), and thus the discrepancy between the two values, as in Eq. (23):

$$e = \frac{H_{2\ produced,Faradaic} - H_{2\ produced,exp}}{H_{2\ produced,Faradaic}} \cdot 100 \tag{23}$$

For the cases 1, 2 and 3 respectively (as in Table II), e resulted to be 4.35 %, 3.02 % and 4.34 %, proving the limited discrepancy between theoretical calculations and experimental outcomes.

3.2. *Local cell voltage and current distribution*

The results from the experimental GC analyses shown in section 3.1 are now utilized to determine the distribution of current density and voltage, as described in section 2.4 and 2.5.

In agreement with the gas analysis discussed in Section 3.1, the models for calculating the local current density (Fig. 6) and voltage also clearly show higher cell activity in the region near the gas inlet section. The calculations highlight a cell voltage above 1.150 V for the areas corresponding to sampling points 1, 2, and 3 for all conditions studied except for condition no.3 (Table VI, Table VII and Table VIII).

In condition no.2, all subsequent points (4–11) exhibit a rather uniform voltage, ranging between 1.085 V and 1.100 V, unlike the case with FF = 300 mL/min, where the highest voltage values are observed in the sections near the outlet. This phenomenon is mainly attributed to the low water content in those same sections – a condition that also occurs in all other cases but to a much lesser extent, such that with FF = 500 mL/min, the phenomenon is not even observed.

The current density is consistent with the voltage profile, highlighting different behaviors between different regions of the cell: values between 0.4 and 0.45 A/cm^2 at points 1, 2, and 3 (about twice as much as the overall cell current density of 0.235 A/cm^2), and below 0.260 A/cm^2 at the remaining points.

Since the current density is an indicator of the electrochemical activity of the cell, it can be stated that the area represented by points 1, 2, and 3 – exhibiting values up to 2 times higher than those of the subsequent regions – is the most active and, consequently, also the most prone to degradation. As also shown in the literature concerning the testing of solid oxide cells [4,5,11,12,15–17], nominal current density values exceeding 0.5 A/cm^2 are rarely reached, if not for accelerated stress tests, and this operating point is therefore considered a threshold that should not be exceeded in order to avoid highly accelerated cell degradation phenomena.

Similar dynamics to those observed with varying inlet flow rate are found when changing the composition of the inlet gas. At equal sampling points, the comparison with tests conducted at lower inlet water content

Table 6
Modelling results for local voltage and current density; as in Table II, condition no.1.

Sampling point	Voltage (V)	Current density (A/cm^2)	Local steam conversion (%)
1	1.202 ± 0.01	0.411 ± 0.012	22.1
2	1.213 ± 0.01	0.441 ± 0.013	23.7
3	1.206 ± 0.01	0.423 ± 0.013	22.8
4	1.123 ± 0.01	0.137 ± 0.004	9.6
5	1.147 ± 0.01	0.172 ± 0.005	13.2
6	1.193 ± 0.01	0.254 ± 0.008	22.5
7	1.156 ± 0.01	0.116 ± 0.003	13.3
8	1.201 ± 0.01	0.187 ± 0.006	24.8
9	1.227 ± 0.01	0.184 ± 0.006	32.4
10	1.241 ± 0.01	0.208 ± 0.006	36.6
11	1.238 ± 0.01	0.202 ± 0.006	35.5

Table 7
Modelling results for local voltage, current density and steam conversion; as in Table II, condition no.2.

Sampling point	Voltage (V)	Current density (A/cm^2)	Local steam conversion (%)
1	1.153 ± 0.01	0.451 ± 0.014	14.5
2	1.151 ± 0.01	0.437 ± 0.013	14.1
3	1.159 ± 0.01	0.461 ± 0.014	14.9
4	1.106 ± 0.01	0.259 ± 0.008	9.8
5	1.085 ± 0.01	0.171 ± 0.005	7.1
6	1.103 ± 0.01	0.206 ± 0.006	9.3
7	1.089 ± 0.01	0.144 ± 0.004	7.2
8	1.089 ± 0.01	0.129 ± 0.004	6.9
9	1.099 ± 0.01	0.143 ± 0.004	8.2
10	1.100 ± 0.01	0.146 ± 0.004	8.4
11	1.096 ± 0.01	0.133 ± 0.004	7.7

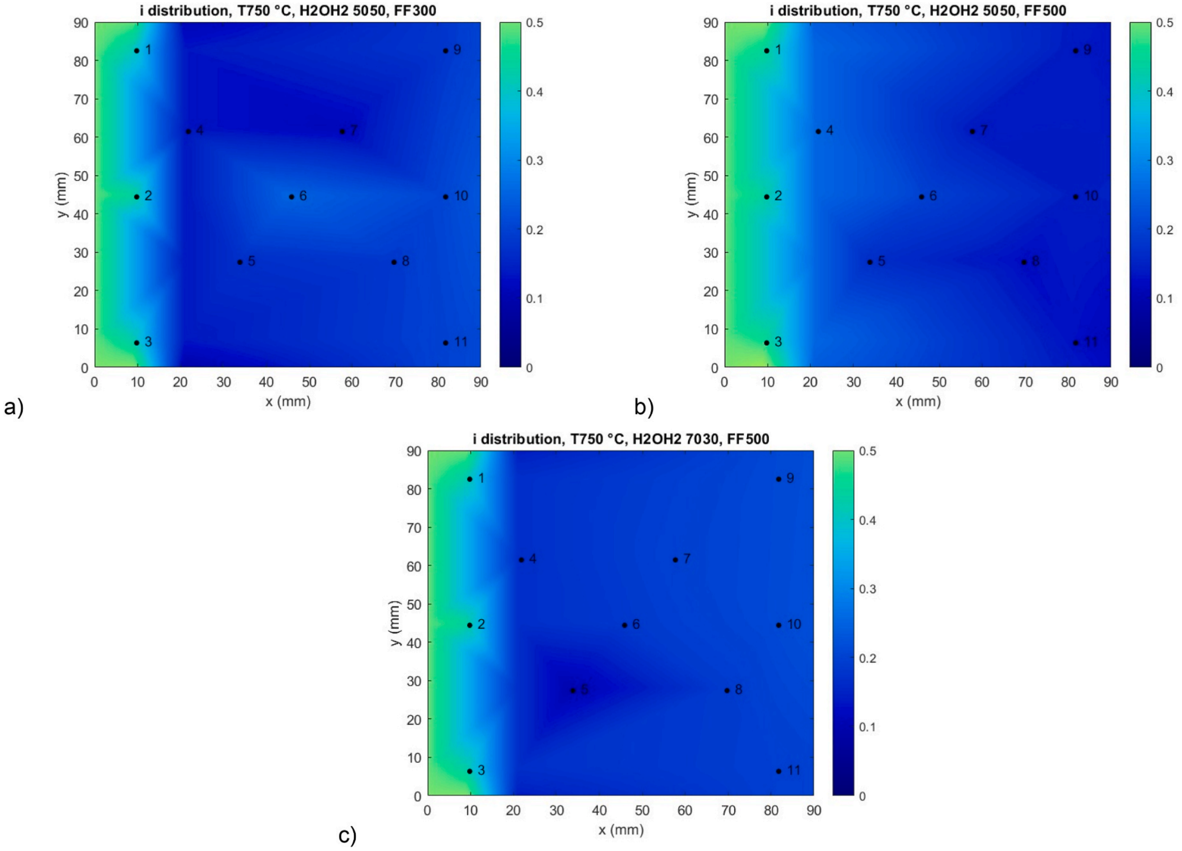

Fig. 6. Contour plot of modelling results for local current density; as in Table II, a) condition no.1; b) condition no.2; c) condition no.3.

Table 8
Modelling results for local voltage, current density and steam conversion; as in Table II, condition no.3.

Sampling point	Voltage (V)	Current density (A/cm^2)	Local steam conversion (%)
1	1.093 ± 0.01	0.422 ± 0.013	9.7
2	1.098 ± 0.01	0.438 ± 0.013	10.1
3	1.095 ± 0.01	0.429 ± 0.013	9.9
4	1.026 ± 0.01	0.170 ± 0.005	4.4
5	1.009 ± 0.01	0.102 ± 0.003	2.7
6	1.039 ± 0.01	0.186 ± 0.006	5.1
7	1.050 ± 0.01	0.201 ± 0.006	5.8
8	1.053 ± 0.01	0.191 ± 0.008	5.9
9	1.071 ± 0.01	0.214 ± 0.006	7.0
10	1.071 ± 0.01	0.215 ± 0.006	7.0
11	1.065 ± 0.01	0.198 ± 0.006	6.5

reveals lower average voltage values, resulting from the higher water concentration at each location. This effect is particularly pronounced in the region near the outlet: the voltages at sampling points 9, 10, and 11 are slightly lower than those at the inlet. In contrast, in the test with $H_2/H_2O = 50/50$ and FF = 300 mL/min, these outlet voltages are slightly higher – despite the lower electrochemical activity – due to the reduced amount of gas (e.g. water) available for conversion.

Similarly to the Faradaic balance, area-weighted local current densities have been compared to the applied global current density to validate internal consistency. By multiplying each local current density (as in Tables VI and VII and VIII) by the corresponding area to which that value is associated, and summing the resulting products, total current values of 18.2 A, 18.3 A, and 18.2 A are obtained for case studies 1, 2, and 3, respectively. These values deviate by approximately 4 % from the 19 A actually applied to the cell. It is worth noting that this deviation is nearly identical to that observed for the hydrogen flow rate at the cell outlet, when comparing theoretical and experimental calculations.

In Tables VI VII, and VIII, error propagation for current density and voltage was considered, based on the measurement uncertainty of the GC from which these modeled quantities are derived. The current density was found to have an error directly proportional to the electrochemical activity, since it is proportionally linked to the GC measurement: the ±3 % error on the GC translates into a ±3 % error on the current density. Therefore, the modeled values of current density can be considered only minimally affected by measurement uncertainties.

Similar considerations can be made regarding the estimated error on voltage. Unlike current density, voltage does not have a direct proportional relationship with experimental measurements and is influenced by multiple sources of error, making its evaluation more complex. The contributing factors include the GC measurement error, temperature measurement uncertainty, and potential uncertainties in model input parameters. Given the large number of variables involved, we focused on the contributions from the GC, temperature, and one key model input parameter—activation energy, assumed with a ±10 % uncertainty – to assess model stability.

Consequently, the error was calculated for each component of the voltage shown in Eq. (1), resulting in an overall estimated uncertainty of approximately ±10 mV for all cases. This uncertainty is largely dominated by the activation energy, which accounts for nearly 50 % of the total error. The estimated voltage uncertainty is considered applicable uniformly across all sampling points.

Since in this study the 0.5 A/cm^2 threshold has not been reached, as suggested by the modeling analysis, it is reasonable not to expect a dramatic degradation of cell performance over the medium to long term. Among the consequences of operating at high current density, numerous studies report the occurrence of Ni migration or Ni re-oxidation – particularly when a high concentration of water vapor is combined with high current density or voltage, leading to fuel-electrode-induced cell degradation in the long term; by contrast, the impact on the air-electrode side is negligible [6,18,55,56].

The nickel re-oxidation reaction is the following [57]:

$$Ni + H_2O \leftrightarrow NiO + H_2 \tag{24}$$

The high water concentration gradient between the inlet area (points 1, 2, and 3) and the immediately subsequent region (point 4), as shown in Fig. 5, leads to a strong imbalance in NiO concentration, with NiO being more concentrated near points 1, 2, and 3 in order to re-establish equilibrium in the reaction (Eq. (24)). This oxide, migrating towards regions of lower concentration (point 4), will further shift the reaction toward the products, accelerating the consumption of Ni and H_2O in the inlet section, ultimately causing a decrease of active sites for the inlet gas.

This phenomenon, on one hand, highlights the degradation mechanism that develops in regions of higher electrochemical activity, and on the other hand explains the greater water consumption observed at the cell surface near the gas inlet. However, despite this observed inlet bias effect is consistent with possible degradation mechanisms, further microstructural characterization would be needed to confirm this.

Other degradation mechanisms of the cell have been observed and reported in numerous studies. Among these, Ni coarsening is one of the most extensively investigated [55,58]. This process involves an increase in the size and a decrease in the number of nickel particles, resulting in a loss of interparticle contact and, consequently, an increase in polarization resistance. Hubert et al. [59] reported a significant occurrence of Ni coarsening in post-mortem analyses following a series of long-term experiments (ranging from 1000 h to 9000 h), leading to a substantial loss of active sites. The phenomenon was particularly pronounced at higher operating temperatures.

Ni migration has also emerged as a frequent degradation pathway, with several studies [55,60,61] confirming its occurrence and detrimental impact on cell performance, especially when associated with a coarser Ni microstructure [62].

The current density gradient across different areas of the cell is a phenomenon also reported in the literature: Yildiz et al. [27] developed a model that shows a decrease from the gas inlet region (about 0.55 A/cm^2) to the outlet region (about 0.38 A/cm^2); similarly, Xu et al. [28] performed a numerical investigation highlighting the same trend (approximately 0.49 A/cm^2 at the inlet and 0.14 A/cm^2 at the outlet), considering an average applied current density of 0.4 A/cm^2. In both examples, however, unlike in the present study, the decrease in current density along the flow direction is nearly linear.

One reason why the imbalance observed in this work is particularly marked can be attributed to the Ni migration and Ni re-oxidation mechanisms discussed earlier, which significantly shift electrochemical activity towards the inlet region – phenomena that are not modeled in the cited references. By contrast, the present study, being supported by experimental data, is able to account for all the phenomena occurring within the system.

Although current density and voltage are closely related, a higher current density does not necessarily correspond to a higher voltage: for instance, in condition no 1, point 1 exhibits 0.411 A/cm^2 and 1.202 V, while point 11 shows 0.202 A/cm^2 and 1.238 V. This behavior can be attributed to the higher water concentration at point 1 compared to point 11, resulting in a lower voltage for the same current density. Moreover, regions near the outlet exhibit a higher voltage than those near the inlet, for the same current density, due to concentration losses.

Local cell performance in SOFCs has been previously investigated using segmented cell and impedance-resolved approaches. Extending these approaches, this work introduces model-derived voltage maps validated by multi-sampling in electrolysis mode, representing a novel methodological contribution.

3.3. Local temperature distribution – FF variation

The temperature distribution is determined as described in Section 2.6.

The experimental temperature measurements inherently account for certain errors due to various factors, including: (i) a sub-optimal insulation of the environment surrounding the cell and a non-uniform temperature distribution caused by thermal resistances within the furnace not being precisely calibrated to the same power level; (ii) non-uniform positioning of thermocouples. To mitigate such systematic errors, a reference measurement was conducted, in which the cell was replaced, in the same test bench, with an insulating material (Thermiculite) of identical dimensions, without applying any gas flow or electrical load. Under these conditions, the recorded temperature reflects only the errors attributable to the furnace and thermocouples. The difference (ΔT) between the temperature measured during the actual experiments (which includes all effects) and that recorded in the reference test thus represents the temperature variation due to fluid dynamic and chemical/electrochemical phenomena. The sum of the nominal operating temperature (750 °C) and ΔT yields a corrected temperature value, effectively compensating for systematic errors introduced by the experimental setup. The temperature values reported in this work are those obtained following the correction.

Based on the defined approach, the calculated values are representative of all local phenomena related to cell operation (e.g., fluid dynamic, chemical and electrochemical processes), but not of boundary-related effects (e.g., cell positioning inside the furnace, non-uniform operation of the furnace's heating elements, etc.).

The results of the analysis are reported in Table IX and Fig. 7, highlighting a few key aspects: (i) the temperature in the inlet zone is the lowest across the entire cell: in agreement with the simulations of local voltage and current density (Tables VI, VII and Table VIII), the high electrochemical activity – combined with operation in endothermic mode ($V < V_{therm}$) – leads to significant heat absorption; (ii) the central and outlet zones exhibit lower electrochemical activity, resulting in reduced heat absorption compared to the inlet sections. Consequently, the gas reaches a temperature lower than that of the surrounding system (750 °C), although it tends to approach it; (iii) experimentally, maximum temperatures slightly higher than that of the furnace are observed. This is not indicative of exothermic operation but rather of imperfect furnace control, which is not precisely centered at 750 °C; (iv) the gas temperature decreases with increasing flow rate, as a higher incoming gas flow – assuming constant cross-sectional area and gas density – results in a higher transit velocity and, therefore, shorter residence time within the furnace; (v) sampling point 10 consistently records lower temperature values compared to the surrounding zones, with differences of up to 15 °C. Given the corrections applied to the experimental data, in principle, no systematic error should be present at that point, although it appears to deviate from the overall trend observed in both the cell and the model. Future developments of this study will aim to investigate this aspect more thoroughly, in order to better understand the underlying cause of the anomaly (e.g., chemical/electrochemical reactions, fluid dynamics specific to the experimental setup, thermocouple measurement error, or other factors); (vi) if temperature point T10 is excluded from the experimental mapping, as highlighted in Fig. 7, a very similar trend is observed between the model results and the experimental data – specifically, a cooler inlet zone and warmer central and outlet regions. Deviations between the model and the experimental results are limited – less than 1 % - thus confirming the consistency between the two.

Table 9
Modelling results for local temperature; as in Table II, condition no.1 (FF = 300 mL/min) and condition no.2 (FF = 500 mL/min).

Sampling point	Temperature – model/experimental [°C] @ H_2O/H_2 = 50/50, FF = 300 mL/min	Temperature – model/experimental [°C] @ H_2O/H_2 = 50/50, FF = 500 mL/min	Temperature – model/experimental [°C] @ H_2O/H_2 = 70/30, FF = 500 mL/min
1	744.8 ± 2/747.6 ± 1	743.1 ± 2/746.6 ± 1	743.2 ± 2/746.4 ± 1
2	745.1 ± 2/749.5 ± 1	743.2 ± 2/748.5 ± 1	743.1 ± 2/748.3 ± 1
3	744.9 ± 2/745.9 ± 1	743.3 ± 2/745.3 ± 1	743.2 ± 2/744.9 ± 1
4	746.5 ± 2/751.1 ± 1	744.1 ± 2/749.9 ± 1	746.8 ± 2/749.7 ± 1
5	746.3 ± 2/750.4 ± 1	745.8 ± 2/749.4 ± 1	747.1 ± 2/749.0 ± 1
6	746.3 ± 2/751.8 ± 1	745.7 ± 2/750.5 ± 1	747.8 ± 2/750.4 ± 1
7	747.5 ± 2/752.4 ± 1	746.7 ± 2/750.9 ± 1	747.1 ± 2/750.8 ± 1
8	747.5 ± 2/750.6 ± 1	747.4 ± 2/749.6 ± 1	747.4 ± 2/749.3 ± 1
9	748.3 ± 2/749.8 ± 1	747.3 ± 2/748.5 ± 1	747.3 ± 2/748.4 ± 1
10	748.5 ± 2/733.6 ± 1	747.3 ± 2/732.8 ± 1	747.3 ± 2/732.3 ± 1
11	748.5 ± 2/748.4 ± 1	747.5 ± 2/747.7 ± 1	747.6 ± 2/747.2 ± 1

Error propagation analysis was also performed for temperature measurements. For the experimental data, the uncertainty is solely attributable to the tolerance of the thermocouples (±1 °C), whereas the modeled values are affected by the tolerances assigned to the model input parameters. By assuming a conservative tolerance of ±10 % for two key parameters in the temperature calculation (h and c_p), the resulting overall uncertainty on temperature is estimated at approximately ± 2 °C, which is considered applicable to all sampling points.

High thermal gradients on the cell surface are well known to be detrimental, as they are a primary cause of irreversible structural damage, such as rupture and cracking [63,64], due to uneven thermal expansion across the cell surface. Thermal gradients within the cell have also been documented in the literature: Lim et al. [65] report a smoothly increasing simulated temperature profile, with a difference between inlet and outlet of approximately 20 °C for a cell operating in exothermic electrolysis mode at $i = 0.6944\ A/cm^2$ and $V = 1.418\ V$. Xu et al. [28] simulate an SOEC at $i = 0.4\ A/cm^2$ and $V = 1.2867\ V$, showing a nearly linear profile and a ΔT of about 9 °C between inlet and outlet. However, comparison is limited due to the assumption of uniform voltage and current density across the entire cell surface made by the aforementioned studies – an assumption not adopted in the present work.

To place the obtained temperature results into context, a review of the literature on thermal gradients in SOCs was conducted. Several studies suggest a structural safety limit of 5 K/cm for the cell [66,67], while Petipas et al. report a value of 10 K/cm [68]. Chen et al. [69] further delineate thresholds by defining a safe range (<5 K/cm), a hazardous range (5–8 K/cm), and a high-risk range (>8 K/cm) for evaluating SOEC safety. In comparison, the gradients measured in this study (≤4.5 °C across the entire cell surface, corresponding to an average of 0.5 K/cm) fall well below these thresholds and can therefore be considered non-critical from this standpoint.

Moreover, a comparison between the present SOEC investigation and previous studies conducted with a similar setup in SOFC mode ([37–39]) reveals notable distinctions between the two operating modes. In SOFC mode, the electrochemical activity was more uniformly distributed along the fuel electrode surface, whereas in SOEC a pronounced activity was observed near the gas inlet, with local current densities reaching up to twice the average value. Such behavior is unique to electrolysis operation, as it induces stronger heterogeneities in gas composition and current density than those typically observed under fuel cell operation. Furthermore, the present study indicates that Ni re-oxidation and migration phenomena, likely exacerbated by steep H_2O/H_2 gradients, represent a degradation pathway specific to electrolysis. Overall, these findings demonstrate that extending the multisampling diagnostic approach to electrolysis mode not only confirms its versatility but also reveals degradation mechanisms not evident in fuel cell operation.

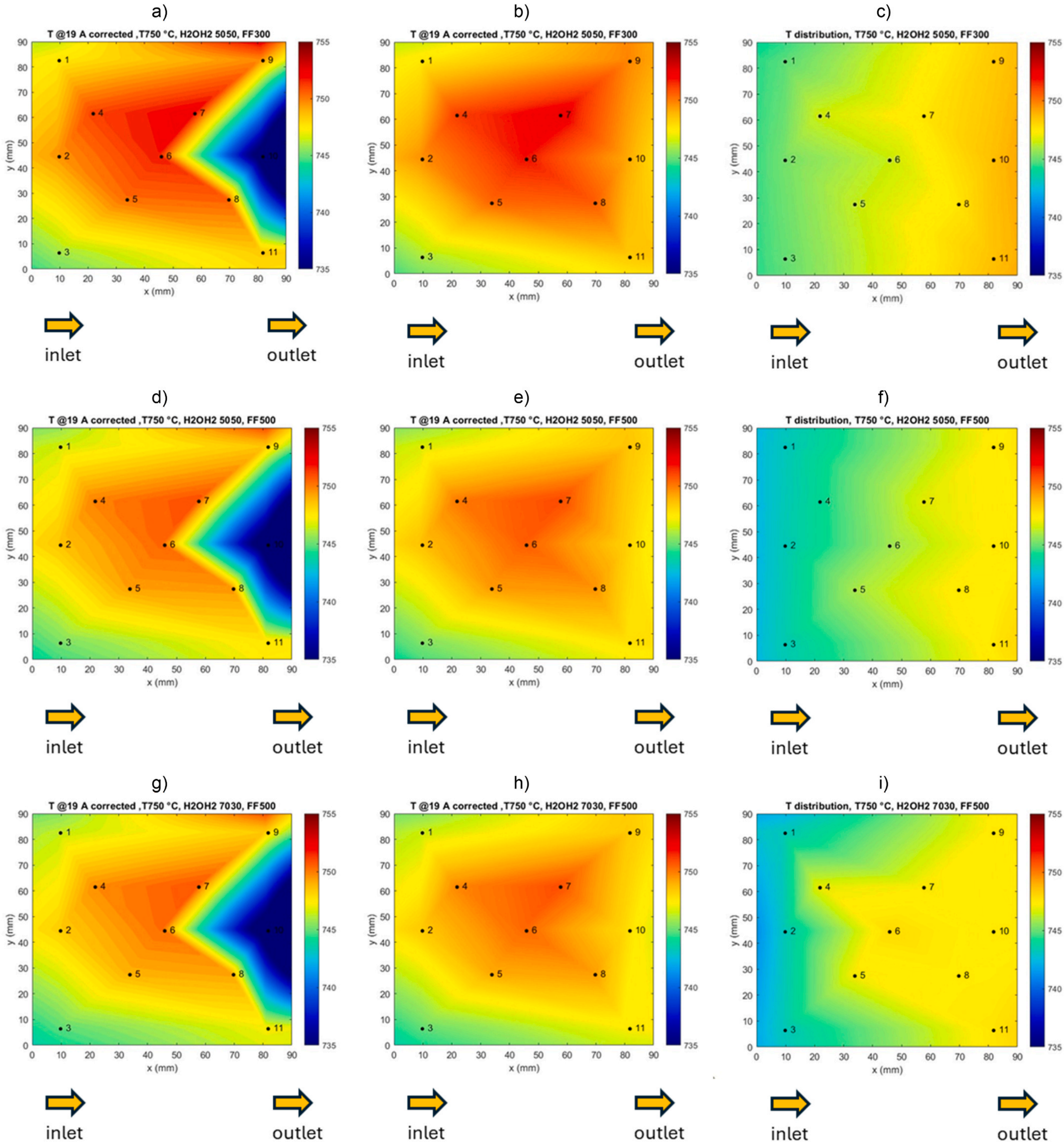

Fig. 7. Temperature distribution contour plots; a) condition no.1, experimental; b) condition no.1, experimental excluding T10; c) condition no.1, model; d) condition no.2, experimental; e) condition no.2, experimental excluding T10; f) condition no.2, model; g) condition no.3, experimental; h) condition no.3, experimental excluding T10; i) condition no.3, model.

4. Conclusion

This study presents an innovative methodology to investigate localized electrochemical and thermal behavior in a commercial 81 cm^2 SOEC, by means of an in-house built multisampling test setup combined with simplified modeling tools. The use of 11 sampling points across the fuel electrode surface allows for in-operando spatial measurements of gas composition and temperature. Such experimental data were used as input parameters for predictive electrochemical–thermal models which proved effective in quantifying local voltage, current density, and temperature distributions.

The cell was operated under a range of inlet fuel compositions and flow conditions, at the constant temperature of 750 °C, and a clear concentration of electrochemical activity in the inlet region was observed in all scenarios, where local current densities reached values up to 0.45 A/cm^2, twice the cell average current density. This non-uniform behavior was directly linked to steep H_2O/H_2 gradients, which also influenced the distribution of cell voltage (up to 1.2 V in the inlet sections). Such activity defines the most exposed regions to long-term degradation phenomena, possibly including Ni re-oxidation, migration and coarsening.

Thermal mapping and model predictions further showed that the inlet region operates at slightly lower temperatures due to endothermic reactions and higher conversion rates, while outlet regions tend towards equilibrium (e.g. furnace temperature). The overall temperature variations across the cell remained modest (<5 °C), and the agreement between experimental and simulated data validates the consistency of the proposed framework. An isolated anomaly observed near the outlet indicates the need for further refinement of the experimental setup, but does not undermine the general trends identified.

Future studies will extend this framework to co-electrolysis and fuel-assisted electrolysis modes, with the aim of further understanding how gas composition and localized gradients shape the performance and stability of SOC technology in multiple operating conditions, and will also include detailed studies on the cell's microstructural and morphological characteristics (e.g., via SEM), in order to better correlate surface features with the localized electrochemical performance observed in this study.

CRediT authorship contribution statement

Francesco Marino: Writing – review & editing, Writing – original draft, Visualization, Validation, Software, Methodology, Investigation, Formal analysis, Data curation, Conceptualization. **Davide Pumiglia:** Visualization, Validation, Project administration, Methodology. **Francesca Santoni:** Writing – review & editing, Validation, Supervision. **Maria Anna Murmura:** Writing – review & editing, Supervision, Software. **Luca Simonetti:** Validation, Supervision. **Viviana Cigolotti:** Writing – review & editing, Resources, Funding acquisition. **Giulia Monteleone:** Resources, Funding acquisition. **Elio Jannelli:** Resources, Funding acquisition.

Declaration of competing interest

The authors declare that they have no known competing financial interests or personal relationships that could have appeared to influence the work reported in this paper.

Acknowledgement

This research was funded by the European Union - NextGenerationEU from the Italian Ministry of Environment and Energy Security, POR H2 AdP MEES/ENEA with involvement of CNR and RSE, PNRR - Mission 2, Component 2, Investment 3.5 “Ricerca e sviluppo sull'idrogeno”, CUP: I83C22001170006.

Data availability

Data will be made available on request.

References

[1] I. Dincer, Green methods for hydrogen production, Int. J. Hydrogen Energy (Jan. 2012) 1954–1971, https://doi.org/10.1016/j.ijhydene.2011.03.173.
[2] M. Yu, K. Wang, H. Vredenburg, Insights into low-carbon hydrogen production methods: green, blue and aqua hydrogen, Int. J. Hydrogen Energy 46 (41) (Jun. 2021) 21261–21273, https://doi.org/10.1016/j.ijhydene.2021.04.016.
[3] L.A. Jolaoso, I.T. Bello, O.A. Ojelade, A. Yousuf, C. Duan, P. Kazempoor, Operational and scaling-up Barriers of SOEC and Mitigation Strategies to Boost H2 production- a Comprehensive Review, Elsevier Ltd., Oct. 15, 2023, https://doi.org/10.1016/j.ijhydene.2023.05.077.
[4] V.N. Nguyen, Q. Fang, U. Packbier, L. Blum, Long-term tests of a Jülich planar short stack with reversible solid oxide cells in both fuel cell and electrolysis modes, Int. J. Hydrogen Energy 38 (11) (Apr. 2013) 4281–4290, https://doi.org/10.1016/j.ijhydene.2013.01.192.
[5] B. Königshofer, et al., Development of test protocols for solid oxide electrolysis cells operated under accelerated degradation conditions, J. Power Sources 497 (Jun. 2021), https://doi.org/10.1016/j.jpowsour.2021.229875.
[6] Q. Shao, et al., Performance evolution analysis of solid oxide electrolysis cells operating at high current densities, Int. J. Hydrogen Energy 57 (Feb. 2024) 709–716, https://doi.org/10.1016/j.ijhydene.2024.01.096.
[7] Z. Liu, J. Hu, A. Wu, Z. Lu, W. Guan, Stability and energy consumption of solid oxide electrolysis cells under wide fluctuating and stable conditions, J. Power Sources 616 (Oct. 2024), https://doi.org/10.1016/j.jpowsour.2024.235113.
[8] C. Yang, Z. Li, Y. Wang, H. Miao, J. Yuan, Multiphysics analysis of flow uniformity and stack/manifold configuration in a kilowatt-class multistack solid oxide electrolysis cell module, Energy 307 (Oct. 2024), https://doi.org/10.1016/j.energy.2024.132627.
[9] G. Sassone, et al., Effect of the operating temperature on the degradation of solid oxide electrolysis cells, J. Power Sources 605 (Jun. 2024), https://doi.org/10.1016/j.jpowsour.2024.234541.
[10] B. Shboul, et al., New hybrid photovoltaic-fuel cell system for green hydrogen and power production: performance optimization assisted with Gaussian process regression method, Int. J. Hydrogen Energy 59 (Mar. 2024) 1214–1229, https://doi.org/10.1016/j.ijhydene.2024.02.087.
[11] X. Zhang, J.E. O'Brien, R.C. O'Brien, J.J. Hartvigsen, G. Tao, G.K. Housley, Improved durability of SOEC stacks for high temperature electrolysis, Int. J. Hydrogen Energy 38 (1) (Jan. 2013) 20–28, https://doi.org/10.1016/j.ijhydene.2012.09.176.
[12] Q. Ma, et al., Electrochemical performances of a solid oxide electrolysis short stack under multiple steady-state and cycling operating conditions, Inorganics (Basel) 12 (11) (Nov. 2024), https://doi.org/10.3390/inorganics12110288.
[13] T. Skafte, J. Løye, P. Hjelm, Blennow, C.R. Graves, General rights quantitative review of degradation and lifetime of solid oxide cells and stacks [Online]. Available: www.EFCF.com/Lib, 2025.
[14] L. Blum, et al., Solid oxide fuel cell, stack and system development status at Forschungszentrum Jülich, ECS Trans. 68 (1) (Jun. 2015) 157–169, https://doi.org/10.1149/06801.0157ecst.
[15] Q. Fang, L. Blum, N.H. Menzler, Performance and degradation of solid oxide electrolysis cells in stack, J. Electrochem. Soc. 162 (8) (2015) F907–F912, https://doi.org/10.1149/2.0941508jes.
[16] J. Beyrami, R.N. Nakashima, A. Nemati, H.L. Frandsen, Lifetime and performance of solid oxide electrolysis stacks and systems under different operation modes and conditions, Int. J. Hydrogen Energy 102 (Feb. 2025) 980–995, https://doi.org/10.1016/j.ijhydene.2025.01.028.
[17] F. Tietz, D. Sebold, A. Brisse, J. Schefold, Degradation phenomena in a solid oxide electrolysis cell after 9000 h of operation, J. Power Sources 223 (Feb. 2013) 129–135, https://doi.org/10.1016/j.jpowsour.2012.09.061.
[18] Y. Wang, W. Li, L. Ma, W. Li, X. Liu, Degradation of Solid Oxide Electrolysis Cells: Phenomena, Mechanisms, and Emerging Mitigation strategies—A Review, Chinese Society of Metals, Oct. 15, 2020, https://doi.org/10.1016/j.jmst.2019.07.026.
[19] M.S. Sohal, A. V Virkar, S.N. Rashkeev, M. V Glazoff, Modeling degradation in solid oxide electrolysis cells [Online]. Available: http://www.inl.gov, 2010.
[20] G. Ju, K. Reifsnider, IMECE2006-13874 DRAFT infrared thermography and thermoelectrical study of a solid oxide fuel cell [Online]. Available: https://proceedings.asmedigitalcollection.asme.org, 2006.
[21] X. Zhang, J.E. O'Brien, R.C. O'Brien, G.K. Housley, Durability evaluation of reversible solid oxide cells, J. Power Sources 242 (2013) 566–574, https://doi.org/10.1016/j.jpowsour.2013.05.134.
[22] S.E. Wolf, V. Vibhu, E. Tröster, I.C. Vinke, R.A. Eichel, L.G.J. de Haart, Steam electrolysis vs. co-electrolysis: Mechanistic studies of long-term solid oxide electrolysis cells, Energies 15 (15) (Aug. 2022), https://doi.org/10.3390/en15155449.
[23] X. Tong, S. Ovtar, K. Brodersen, P.V. Hendriksen, M. Chen, A 4 × 4 cm2 nanoengineered solid oxide electrolysis cell for efficient and durable hydrogen production, ACS Appl. Mater. Interfaces 11 (29) (Jul. 2019) 25996–26004, https://doi.org/10.1021/acsami.9b07749.
[24] J. Schefold, A. Brisse, H. Poepke, 23,000 h steam electrolysis with an electrolyte supported solid oxide cell, Int. J. Hydrogen Energy 42 (19) (May 2017) 13415–13426, https://doi.org/10.1016/j.ijhydene.2017.01.072.
[25] H. Chen, J. Wang, X. Xu, Parametric study of operating conditions on performances of a solid oxide electrolysis cell, J. Therm. Sci. 32 (6) (Nov. 2023) 1973–1988, https://doi.org/10.1007/s11630-023-1772-4.
[26] Q. Hou, C. Guan, G. Xiao, J.Q. Wang, Z. Zhu, Effect of oxygen partial pressure on solid oxide electrolysis cells, Wuli Huaxue Xuebao/Acta Phys. - Chim. Sin. 35 (3) (2019) 284–291, https://doi.org/10.3866/PKU.WHXB201804171.
[27] Thermal-fluid and electrochemical modeling and performance study of a planar solid oxide electrolysis cell: analysis on SOEC resistances, size, and inlet flow conditions [Online]. Available: www.anl.gov.
[28] Z. Xu, X. Zhang, G. Li, G. Xiao, J.Q. Wang, Comparative performance investigation of different gas flow configurations for a planar solid oxide electrolyzer cell, Int. J. Hydrogen Energy 42 (16) (Apr. 2017) 10785–10801, https://doi.org/10.1016/j.ijhydene.2017.02.097.
[29] Y. Xu, J. Zhang, Z. Tu, Numerical simulation of flow channel geometries optimization for the planar solid oxide electrolysis cell, Int. J. Hydrogen Energy 52 (Jan. 2024) 288–301, https://doi.org/10.1016/j.ijhydene.2023.07.242.
[30] C. Schluckner, V. Subotić, S. Preißl, C. Hochenauer, Numerical analysis of flow configurations and electrical contact positions in SOFC single cells and their impact on local effects, Int. J. Hydrogen Energy 44 (3) (Jan. 2019) 1877–1895, https://doi.org/10.1016/j.ijhydene.2018.11.132.

[31] G. Schiller, W.G. Bessler, K.A. Friedrich, S. Gewies, C. Willich, Spatially resolved electrochemical performance in a segmented planar SOFC, ECS Trans. 17 (1) (May 2009) 79–87, https://doi.org/10.1149/1.3142737.

[32] Y. Wu, H. Liu, Y. Wang, L. An, X. Xu, Spatially resolved electrochemical performance and temperature distribution of a segmented solid oxide fuel cell under various hydrogen dilution ratios and electrical loadings, J. Power Sources 536 (Jul. 2022), https://doi.org/10.1016/j.jpowsour.2022.231477.

[33] M.W. Kim, M.J. Son, H. Park, J.Y. Park, H.T. Lim, Experimental investigation of In-plane performance variation on anode supported solid oxide fuel cells using segmented cathodes and reference electrodes, Fuel Cells 20 (2) (Apr. 2020) 212–219, https://doi.org/10.1002/fuce.201900214.

[34] M. Lang, C. Bohn, M. Henke, G. Schiller, C. Willich, F. Hauler, Understanding the current-voltage behavior of high temperature solid oxide fuel cell stacks, J. Electrochem. Soc. 164 (13) (2017) F1460–F1470, https://doi.org/10.1149/2.1541713jes.

[35] H. Moussaoui, A. Wesoly, S. Diethelm, Z. Wuillemin, D. Montinaro, J. Van herle, Local electrochemical and thermal investigation of a segmented reversible solid oxide fuel cell and electrolyzer, Electrochim. Acta 475 (Jan. 2024), https://doi.org/10.1016/j.electacta.2023.143627.

[36] B. Königshofer, M. Höber, N.H. Menzler, H. Schröttner, C. Hochenauer, V. Subotić, Experimental investigation of segmented SOECs: locally-resolved impedance and degradation characteristics, Int. J. Hydrogen Energy 48 (10) (Feb. 2023) 3740–3758, https://doi.org/10.1016/j.ijhydene.2022.10.265.

[37] F. Santoni, et al., In-situ study of the gas-phase composition and temperature of an intermediate-temperature solid oxide fuel cell anode surface fed by reformate natural gas, J. Power Sources 370 (Dec. 2017) 36–44, https://doi.org/10.1016/j.jpowsour.2017.09.078.

[38] D. Pumiglia, et al., SOFC anode process characterization by means of a spot-sampling Set-up for in-Operando gas analysis, ECS Trans. 75 (49) (Jan. 2017) 1–8, https://doi.org/10.1149/07549.0001ecst.

[39] B. Conti, B. Bosio, S.J. McPhail, F. Santoni, D. Pumiglia, E. Arato, A 2-D model for intermediate temperature solid oxide fuel cells preliminarily validated on local values, Catalysts 9 (1) (Jan. 2019), https://doi.org/10.3390/catal9010036.

[40] D.M. Silva-Mosqueda, F. Elizalde-Blancas, D. Pumiglia, F. Santoni, C. Boigues-Muñoz, S.J. McPhail, Intermediate temperature solid oxide fuel cell under internal reforming: critical operating conditions, associated problems and their impact on the performance, Appl. Energy 235 (Feb. 2019) 625–640, https://doi.org/10.1016/j.apenergy.2018.10.117.

[41] *High temperature electrolysis*, vol. 95, in: M.A. Laguna-Bercero (Ed.), Lecture Notes in Energy, vol. 95, Springer International Publishing, Cham, 2023, https://doi.org/10.1007/978-3-031-22508-6.

[42] F.R. Bianchi, A. Baldinelli, L. Barelli, G. Cinti, E. Audasso, B. Bosio, Multiscale modeling for reversible solid oxide cell operation, Energies 13 (19) (Oct. 2020), https://doi.org/10.3390/en13195058.

[43] A. Alzahrani, I. Dincer, X. Li, A performance assessment study on solid oxide fuel cells for reduced operating temperatures, Int. J. Hydrogen Energy 40 (24) (Jun. 2015) 7791–7797, https://doi.org/10.1016/j.ijhydene.2014.11.115.

[44] M. Ni, M.K.H. Leung, D.Y.C. Leung, A modeling study on concentration overpotentials of a reversible solid oxide fuel cell, J. Power Sources 163 (1) (Dec. 2006) 460–466, https://doi.org/10.1016/j.jpowsour.2006.09.024. SPEC. ISS.

[45] X. Zhang, L. Wang, M. Espinoza, T. Li, M. Andersson, Numerical simulation of solid oxide fuel cells comparing different electrochemical kinetics, Int. J. Energy Res. 45 (9) (Jul. 2021) 12980–12995, https://doi.org/10.1002/er.6628.

[46] S. Youcef, Z. Bariza, H. Ben Moussa, Y. Sahli, B. Zitouni, H. Ben-Moussa, Solid oxide fuel cell thermodynamic study [Online]. Available: https://www.researchgate.net/publication/321851052, 2017.

[47] I. Celik, S.R. Pakalapati, M.D. Salazar-Villalpando, Theoretical calculation of the electrical potential at the electrode/electrolyte interfaces of solid oxide fuel cells, J. Fuel Cell Sci. Technol. 2 (4) (Nov. 2005) 238–245, https://doi.org/10.1115/1.2039956.

[48] Y. Sun, et al., Solid oxide electrolysis cell under real fluctuating power supply with a focus on thermal stress analysis, Energy 261 (Dec. 2022), https://doi.org/10.1016/j.energy.2022.125096.

[49] M. Naeij, A. Bahari, H. Rajaei Litkohi, M. Soleimani Moghaddam, The role of cerium-based metal-organic frameworks in enhancing palladium nanoparticles for formic acid electrooxidation, Int. J. Hydrogen Energy 156 (Aug. 2025), https://doi.org/10.1016/j.ijhydene.2025.150438.

[50] M. Soleimani Moghaddam, A. Bahari, H. Rajaei Litkohi, Designing and modeling fuel cells made of mixed transition metal dichalcogenide and carbon-based nanostructure electrodes for renewable energy storage, J. Power Sources 604 (Jun. 2024), https://doi.org/10.1016/j.jpowsour.2024.234514.

[51] G. Min, S. Choi, J. Hong, A Review of Solid Oxide steam-electrolysis Cell Systems: Thermodynamics and Thermal Integration, Elsevier Ltd, Dec. 15, 2022, https://doi.org/10.1016/j.apenergy.2022.120145.

[52] D. Sánchez, A. Muñoz, T. Sánchez, An assessment on convective and radiative heat transfer modelling in tubular solid oxide fuel cells, J. Power Sources 169 (1) (Jun. 2007) 25–34, https://doi.org/10.1016/j.jpowsour.2007.01.076.

[53] Yunus A. Çengel, Afshin J. Ghajar, Heat Mass Tran. (2015).

[54] J.H. Lienhard, A heat transfer textbook Fifth Edition [Online]. Available: http://ahtt.mit.edu.

[55] X. Shao, R.A. Budiman, T. Sato, M. Yamaguchi, T. Kawada, K. Yashiro, Review of Factors Affecting the Performance Degradation of Ni-YSZ Fuel Electrodes in Solid Oxide Electrolyzer Cells, Elsevier B.V., Jul. 30, 2024, https://doi.org/10.1016/j.jpowsour.2024.234651.

[56] X. Sun, P.V. Hendriksen, M.B. Mogensen, M. Chen, Degradation in solid oxide electrolysis cells during long term testing, Fuel Cells 19 (6) (Dec. 2019) 740–747, https://doi.org/10.1002/fuce.201900081.

[57] T. Le Cheng, et al., Oxidation of nickel in solid oxide cells during electrochemical operation: experimental evidence, theoretical analysis, and an alternative hypothesis on the nickel migration, J. Power Sources 569 (Jun. 2023), https://doi.org/10.1016/j.jpowsour.2023.232991.

[58] G. Schiller, A. Ansar, M. Lang, O. Patz, High temperature water electrolysis using metal supported solid oxide electrolyser cells (SOEC), J. Appl. Electrochem. 39 (2) (Feb. 2009) 293–301, https://doi.org/10.1007/s10800-008-9672-6.

[59] M. Hubert, J. Laurencin, P. Cloetens, B. Morel, D. Montinaro, F. Lefebvre-Joud, Impact of nickel agglomeration on solid oxide cell operated in fuel cell and electrolysis modes, J. Power Sources 397 (Sep. 2018) 240–251, https://doi.org/10.1016/j.jpowsour.2018.06.097.

[60] Z. Jiao, et al., Integrated 3D modeling unravels the measures to mitigate nickel migration in solid oxide fuel/electrolysis cells, J. Mater. Chem. A Mater. 12 (1) (Nov. 2023) 162–173, https://doi.org/10.1039/d3ta06563d.

[61] Y. Wang, et al., Ni migration of Ni-YSZ electrode in solid oxide electrolysis cell: an integrated model study, J. Power Sources 516 (Dec. 2021), https://doi.org/10.1016/j.jpowsour.2021.230660.

[62] Á. Triviño-Peláez, D. Cademartori, M. Hubert, L. Rorato, M. Prioux, J. Laurencin, Modelling the impact of Ni migration and coarsening on the Ni-YSZ electrodes performances based on three-dimensional microstructures, Electrochim. Acta 520 (Apr. 2025), https://doi.org/10.1016/j.electacta.2025.145791.

[63] H. Wang, et al., Performance and thermal stress evaluation of full-scale SOEC stack using multi-physics modeling method, Energies 16 (23) (Dec. 2023), https://doi.org/10.3390/en16237720.

[64] M. Xu, et al., Modeling of an anode supported solid oxide fuel cell focusing on thermal stresses, Int. J. Hydrogen Energy 41 (33) (Sep. 2016) 14927–14940, https://doi.org/10.1016/j.ijhydene.2016.06.171.

[65] K. Lim, Y. Kim, H. Salihi, H. Ju, Integrated modeling of electrochemical, thermal, and structural behavior in solid oxide electrolysis cells, Int. J. Heat Mass Tran. 224 (Jun. 2024), https://doi.org/10.1016/j.ijheatmasstransfer.2024.125235.

[66] Z. Liang, S. Chen, M. Ni, J. Wang, M. Li, A novel control strategy to neutralize internal heat source within solid oxide electrolysis cell (SOEC) under variable solar power conditions, Appl. Energy 371 (Oct. 2024), https://doi.org/10.1016/j.apenergy.2024.123669.

[67] Y. Wang, A. Banerjee, O. Deutschmann, Dynamic behavior and control strategy study of CO2/H2O co-electrolysis in solid oxide electrolysis cells, J. Power Sources 412 (Feb. 2019) 255–264, https://doi.org/10.1016/j.jpowsour.2018.11.047.

[68] F. Petipas, A. Brisse, C. Bouallou, Thermal management of solid oxide electrolysis cell systems through air flow regulation, Chem. Eng. Trans. 61 (2017) 1069–1074, https://doi.org/10.3303/CET1761176.

[69] H. Chen, T. Wu, S. Luo, Y. Wang, X. Xu, Operating strategy investigation of a solid oxide electrolysis cell under large scale transient electrical inputs, Energy Convers. Manag. 294 (Oct. 2023), https://doi.org/10.1016/j.enconman.2023.117596.